


Article

# Assessing the Performance of ICESat-2/ATLAS Multi-Channel Photon Data for Estimating Ground Topography in Forested Terrain

Yanqiu Xing<sup>1</sup>, Jiapeng Huang<sup>1,\*</sup> , Armin Gruen<sup>2</sup> and Lei Qin<sup>1</sup>

<sup>1</sup> Centre for Forest Operations and Environment, Northeast Forestry University, Harbin 150040, China; yanqiuqing@nefu.edu.cn (Y.X.); qinlei@nefu.edu.cn (L.Q.)

<sup>2</sup> Institute of Theoretical Physics, Federal Institute of Technology (ETH), 8092 Zurich, Switzerland; armin.gruen@geod.baug.ethz.ch

\* Correspondence: huangjp@nefu.edu.cn; Tel.: +86-13946053718

Received: 26 May 2020; Accepted: 26 June 2020; Published: 29 June 2020



**Abstract:** As a continuation of Ice, Cloud, and Land Elevation Satellite-1 (ICESat-1), the ICESat-2/Advanced Topographic Laser Altimeter System (ATLAS) employs a micro-pulse multi-beam photon counting approach to produce photon data for measuring global terrain. Few studies have assessed the accuracy of different ATLAS channels in retrieving ground topography in forested terrain. This study aims to assess the accuracy of measuring ground topography in forested terrain using different ATLAS channels and the correlation between laser intensity parameters, laser pointing angle parameters, and elevation error. The accuracy of ground topography measured by the ATLAS footprints is evaluated by comparing the derived Digital Terrain Model (DTM) from the ATL03 (Global Geolocated Photon Data) and ATL08 (Land and Vegetation Height) products with that from the airborne Light Detection And Ranging (LiDAR). Results show that the ATLAS product performed well in the study area at all laser intensities and laser pointing angles, and correlations were found between the ATLAS DTM and airborne LiDAR DTM (coefficient of determination— $R^2 = 1.00$ , root mean squared error—RMSE = 0.75 m). Considering different laser intensities, there is a significant correlation between the tx\_pulse\_energy parameter and elevation error. With different laser pointing angles, there is no significant correlation between the tx\_pulse\_skew\_est, tx\_pulse\_width\_lower, tx\_pulse\_width\_upper parameters and the elevation error.

**Keywords:** ATLAS; ground topography in forested terrain; laser intensity; laser pointing angle

## 1. Introduction

The spatial structure of forested terrain is listed as an important indicator for monitoring carbon stocks by the International Union of Forest Research Organizations (IUFRO) [1,2]. Assessing ground topography in forested terrain is a prerequisite to accurately determine the forest spatial structure; therefore, high spatial resolution modeling is necessary to characterize forest ecosystems [3,4]. Most optical remote sensing systems can measure ground topography in forested terrain; however, they have poor measurement accuracy (elevation difference = 2.9 m to 4.9 m) [5,6]. Spaceborne [7], airborne [8,9], and terrestrial [10,11] Light Detection And Ranging (LiDAR) systems have shown great potential for acquiring accurate topographic information in this field. Although airborne and terrestrial LiDAR can accurately quantify ground topography in forested terrain, these methods remain largely impractical at large spatial scales due to high data acquisition costs [8,12–14]. Spaceborne LiDAR is unique since it comes with low acquisition costs and provides a synoptic perspective of certain plot-level details from orbit [15].

The Ice, Cloud, and land Elevation satellite-1 (ICESat-1) [16], the Global Ecosystem Dynamics Investigation (GEDI) [17], and the Ice, Cloud, and land Elevation satellite-2 (ICESat-2) [18] are typical spaceborne LiDAR systems. ICESat-1 and GEDI carry large-footprint and waveform LiDAR systems. The Geoscience Laser Altimeter System (GLAS) instrument aboard ICESat-1 was launched in 2003 and decommissioned in 2009 [19]. GLAS is the first spaceborne LiDAR instrument designed to make global observations. GLAS operates a single laser beam from a ~600 km orbit at 40 Hz and has a 70 m diameter footprint and a ~170 m sampling rate along track.

GLAS waveform data has been successfully used to estimate the vertical structure of forest terrain, including ground topography and canopy heights [19–21]. Harding et al. [20] found that the waveform was an accurate representation of the canopy height distribution within a GLAS footprint. Lefsky et al. [21] observed that the models combining GLAS waveforms and Shuttle Radar Topography Mission (SRTM) could explain ~59%–68% of the variance in the field-measured forest canopy height (root mean squared error—RMSE = 4.85–12.66 m); however, sloped ground in forested terrain reduced the canopy height accuracy by using waveform data. Chen [22] found that the ground topography in forested terrain was the critical factor affecting the accurate measurement of canopy height using waveform data, and with increasing forest terrain complexity, the accuracy of estimating forest canopy height decreased. Fang et al. [23] found that in forested terrain with complex ground topography, the GLAS waveform was characterized by multiple energy peaks, in which the ground topography might be broadened and mixed, making the extraction of canopy height difficult. In order to quantify the influence of ground topography on canopy height estimation using GLAS waveform data, Lee et al. [24] found that without slope correction, the canopy height could be overestimated by 3 m over a 15 degree slope. Removing the ground topography in forested terrain from large LiDAR footprint could improve the accuracy of canopy height estimates. Claudia et al. [25] revealed that GLAS height estimates were accurate for areas with a slope up to 10 degrees, whereas the waveform results for areas above 15 degrees were problematic. Ten-to-fifteen degree slopes have been found to be a critical crossover point. The aforementioned studies demonstrated that it was feasible to extract ground topography in forested terrain and canopy height from spaceborne waveform data at stand level; however, the accuracy of canopy height estimation was largely determined by the ground topography, and extracting canopy height across a large LiDAR footprint using waveform data over hilly or mountainous regions is a great challenge. The GEDI was launched on 5 December 2018; however, the GEDI spaceborne data has just recently been released, and no related study was found [26].

The Advanced Topographic Laser Altimeter System (ATLAS) instrument aboard ICESat-2 was launched on 15 September 2018, and data was released on 30 May 2019. ATLAS is the first spaceborne photon-counting LiDAR instrument designed for continuous global observation of Earth [27–29]. Different from the GLAS waveform-digitizing LiDAR system, ATLAS only responds to the presence of return signals and records the time tags with an output of 0 or 1; however, it does not record the return waveform [30–32]. ATLAS operates six laser beams from a ~600 km orbit at 10 kHz and has a footprint (17 m in diameter) sampling rate of ~0.7 m along-track [33,34]. The center-to-center spacing along a track for ATLAS is narrower than that of GLAS (170 m). The high repetition rate enables ATLAS to obtain nearly continuous tracking information, which is necessary to measure the ground topography in forested terrain. While the GLAS LiDAR system uses a laser beam, the ATLAS configuration uses a diffractive optical element to split the laser into six beams arranged as three beam pairs, each of which consists of a strong and weak energy beam at a 4:1 ratio, allowing for local slope determination between each beam pair as well as compensation for varying surface reflectance [27,33,34]. The travel time of each detected photon is used to determine a unique XYZ location on the Earth's surface [35,36]. After ATLAS data was released, Neuenschwander found good correlations between matching Digital Terrain Model (DTM) from airborne LiDAR data and ATLAS data ( $R^2 = 0.99$ , RMSE = 0.85 m) [37]. Wang et al. found that the overall mean difference and RMSE values between the ground elevations retrieved from the ICESat-2 data and the airborne LiDAR-derived ground elevations are -0.61 m and 1.96 m, respectively [38]. However, he primarily examined the retrieved canopy height accuracy from

the ICESat-2 strong beam and did not analyze the accuracy of the ICESat-2 weak beam. Under the same orbital conditions, ATLAS can acquire more continuous photon cloud data using the six-beam instrument with different laser pointing angles and laser intensities. The measurement accuracy of the different ATLAS channels remains to be quantified [39]. To the authors' knowledge, only a few studies have been carried out to analyze the multi-beam geometrical features for measuring ground topography in forested terrain from photon-counting data onboard ICESat-2. Therefore, the effective quantifying of the ground topography in forested terrain using the six-beam photon-counting data is essential to quantify the performance of the unique photon-counting instrument onboard ICESat-2.

The objective of this study is to assess the performance of the ICESat-2/ATLAS multi-channel photon data for estimating ground topography in forested terrain by comparing the derived ground topography from different ATLAS beam photon-counting data with that from Goddard's LiDAR, Hyperspectral and Thermal imager (G-LiHT) data. The paper also analyzes the correlation between laser intensity parameters, laser pointing angle parameters, and estimated ground topography error in forested terrain.

## 2. Materials and Methods

### 2.1. Study Area

The study area ( $33.564^{\circ}\text{N}$ ,  $81^{\circ}684'\text{W}$ ) is a forested area within the City of Aiken, South Carolina, USA (Figure 1). Vegetation footprint types in the study area include cultivated land (0.04%), forest (88.52%), shrubland (0.51%), wetland (6.97%), and artificial surfaces (3.95%) [39]. The upland forest has many tree species, including sand post oak (*Quercus margaretta*), loblolly pine, water oak (*Quercus nigra*), hickory (*Carya*), and turkey oak (*Quercus laevis*) [40]. The elevation of the study area ranges from 91 m to 164 m. Vegetation coverage in the study area ranges from 25% to 66%.

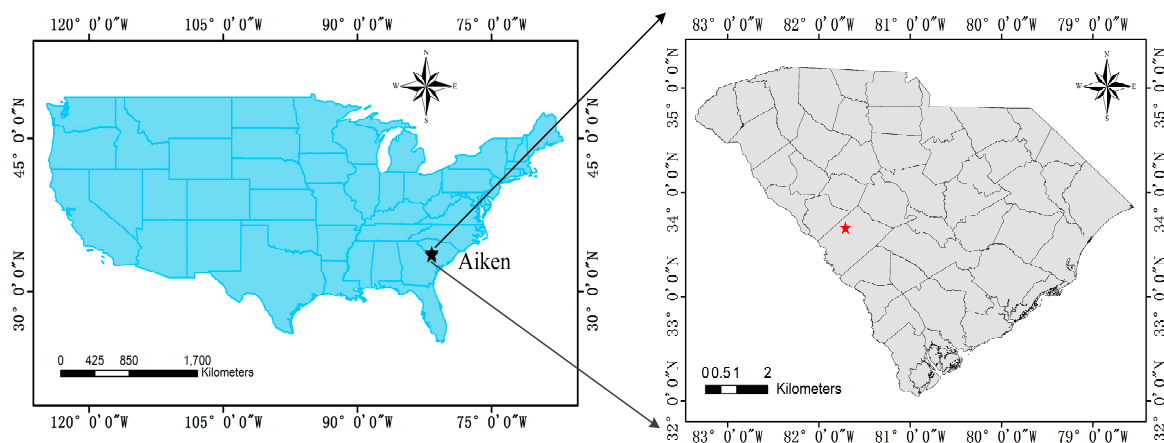


**Figure 1.** Location of the study area at the national and state levels. Figure 1 shows a part of the study site using an image of a USA map. The left part of the image shows the location of the study area in the USA, the right part shows it relative to South Carolina.

### 2.2. Data

The ICESat-2 mission produces along-track ground topography in forested terrain that includes telemetry data (ATL00), reformatted telemetry (ATL01), science unit converted telemetry (ATL02), global geolocated photon data (ATL03), land vegetation elevation (ATL08), and a land/canopy grid (ATL18) [37–41]. ATL00, ATL01, and ATL02 are original photon data sets without scientific algorithms. ATL03 is the geolocated photon cloud and serves as the input data for each of the higher-level data products such as ATL08 and ATL18. The ATL08 algorithm was developed specifically for the extraction of terrain and canopy heights from the ATL03 photon cloud data, and the ATL08 geophysical data product has a 100 m step size in the along-track direction [33]. The ATL03 product not only includes

latitude, longitude, height, and signal photon confidence level of each received photon, but also includes tx\_pulse\_energy, tx\_pulse\_skew\_est, tx\_pulse\_width\_lower, and tx\_pulse\_width\_upper parameters, which may be related to laser intensity and laser pointing angle [37]. All ICESat-2 data products were acquired from <https://search.earthdata.nasa.gov>.

Here the ATL03 product parameters were used, including lat\_ph, lon\_ph, h\_ph, geoid, delta\_time, signal\_conf\_ph, sc\_orient, tx\_pulse\_energy, tx\_pulse\_skew\_est, tx\_pulse\_width\_lower, and tx\_pulse\_width\_upper. The names and corresponding descriptions of product parameters are listed in Table 1 [37–39]. In order to reduce the influence of noise photons in forested terrain ground topography measurement, a signal\_conf\_ph of 4 was used as the signal photon parameter evaluation standard.

**Table 1.** The statistical indicators of global geolocated photon (ATL03) data [39].

ATL03 Product Parameter Name	Description
lat_ph	Latitude of each received photon. Computed from the ECF Cartesian coordinates of the bounce point.
lon_ph	Longitude of each received photon. Computed from the ECF Cartesian coordinates of the bounce point.
h_ph	Height of each received photon, relative to the WGS-84 ellipsoid.
geoid	Geoid height above WGS-84 reference ellipsoid (range −107 to 86 m).
delta_time	Elapsed seconds from the ATLAS SDP GPS Epoch, corresponding to the transmit time of the reference photon.
signal_conf_ph	Confidence level associated with each photon event selected as signal. 0 = noise. 1 = added to allow for buffer but algorithm classifies as background; 2 = low; 3 = med; 4 = high).
sc_orient	This parameter tracks the spacecraft orientation between forward, backward and transitional flight modes.
tx_pulse_energy	The average transmit pulse energy, measured by the internal laser energy monitor, split into per-beam measurements.
tx_pulse_skew_est	The difference between the averages of the lower and upper threshold crossing times. This is an estimate of the transmit pulse skew.
tx_pulse_width_lower	The average distance between the lower threshold crossing times measured by the Start Pulse Detector.
tx_pulse_width_upper	The average distance between the upper threshold crossing times measured by the Start Pulse Detector.

A diagram of ICESat-2 for estimating ground topography in forested terrain is illustrated in Figure 2. The forward orientation (sc\_orient=1) corresponds to ATLAS traveling along the +x direction in the ATLAS instrument reference frame [41–43]. The ATLAS signal photon shown in the yellow square represents the photons detected from the gt3r laser channel. The ATLAS footprint shown in the red square represents the photons detected from the gt3l laser channel. The number of photons in the gt3l channel is less than in the gt3r channel, which is due to the backward orientation of ATLAS [43]. The photon level in the along-track direction was selected to calculate the ground topography in forested terrain. In the right figures, the two laser beams are 90 m apart. The ground topography measured by the two laser beams is similar, and the terrain elevation ranges from 130 m–145 m.

Due to the influence of sunlight as well as atmospheric and system noise, a large number of noise photons are present in the ATLAS data, which seriously reduce the ground elevation measurement accuracy. In order to improve the estimation accuracy of ATLAS photon data, NASA proposed a Differential, Regressive, and Gaussian Adaptive Nearest Neighbor (DRAGANN) method and ATL08 data classified algorithm to filter out noise photon data and classify ground photons [41–43]. In order to explore the estimation accuracy of forested terrain from ATLAS data, this contribution chose to associate the ATL08 classified label with the ATL03 photon data and used the ground signal photons flag mentioned in ATL08 as ground photons to establish an ATLAS-based DTM (Table 2) [37].

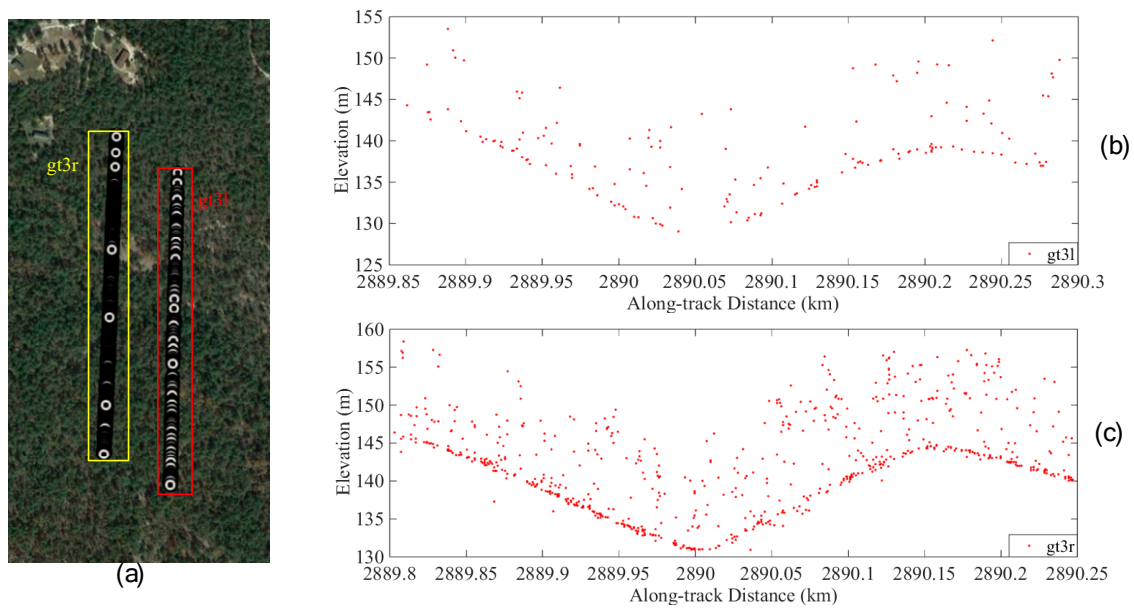


**Figure 2.** (a) The location of gt3r and gt3l data in site 1, City of Aiken, USA. gt3r photons (yellow) and gt3l photons (red) show the location of the Ice, Cloud, and Land Elevation Satellite-2 (ICESat-2) track in Google Earth for context [43]. This illustration only includes signal photons (signal\_conf\_ph=4) and is located in City of Aiken, USA. (b): Profile of ATL03 photons from the weak beam (gt3l). This data was collected on 26 December 2018 at 05:31. (c): Profile of ATL03 photons from the strong beam (gt3r), which has a greater number of signal photons above the surface than in gt3l.

**Table 2.** The statistical indicators of land vegetation elevation (ATL08) product [42].

ATL08 Product Parameter Name	Description
classed_pc_flag	Land Vegetation ATBD classification flag for each photon as either noise, ground, canopy, and top of canopy. 0 = noise, 1 = ground, 2 = canopy, or 3 = top of canopy.
classed_pc_indx	The unique identifier for tracing each ATL08 signal photon to the corresponding photon record on ATL03 is the segment_id, orbit, cycle, and classed_pc_indx.
ph_segment_id	Segment ID of photons tracing back to specific 20 m segment_id on ATL03. The unique identifier for tracing each ATL08 signal photon to the photon on ATL03 is the segment_id, orbit, and classed_pc_indx. The unique identifier for tracing each ATL08 signal photon to the corresponding photon record on ATL03 is the segment_id, orbit, cycle, and classed_pc_indx.

To assess the accuracy of the six beam-ATLAS DTM, the DTM obtained from the ATLAS data was compared with airborne discrete-return LiDAR data, collected for the same longitude and latitude using the multi-sensor instrument G-LiHT [44]. G-LiHT provides distributed laser pulses for measuring ground topography and canopy heights (Table 3) [45].

**Table 3.** The Goddard’s LiDAR, Hyperspectral and Thermal imager (G-LiHT) product levels [44].

G-LiHT Product	Product Level
Trajectory data	Level 1
Classified return data	Level 2
Above Ground Level (AGL) height	Level 2
LiDAR returns	Level 3
DTM	Level 3
Canopy Height Model (CHM)	Level 3

Both Level 2 and Level 3 products along the flight transects were generated from airborne LiDAR data from the G-LiHT science team. The DTM has a 1 m-resolution and was



released as a Tag Image File Format (TIFF) profile. The DTM was assessed to validate the ground topography accuracy [44,45]. The trajectory of the G-LiHT KML (Keyhole Markup Language) data (blue line) and ATLAS data (green line) illustrates the location of the study area of the NASA EARTHDATA (Figure 3). This illustration also includes two G-LiHT DTM profiles used in the study, AMIGACarb\_Augusta\_FIA\_Sep2011\_116s597\_DTM.tif and AMIGACarb\_Augusta\_FIA\_Sep2011\_140s557\_DTM.tif, respectively.

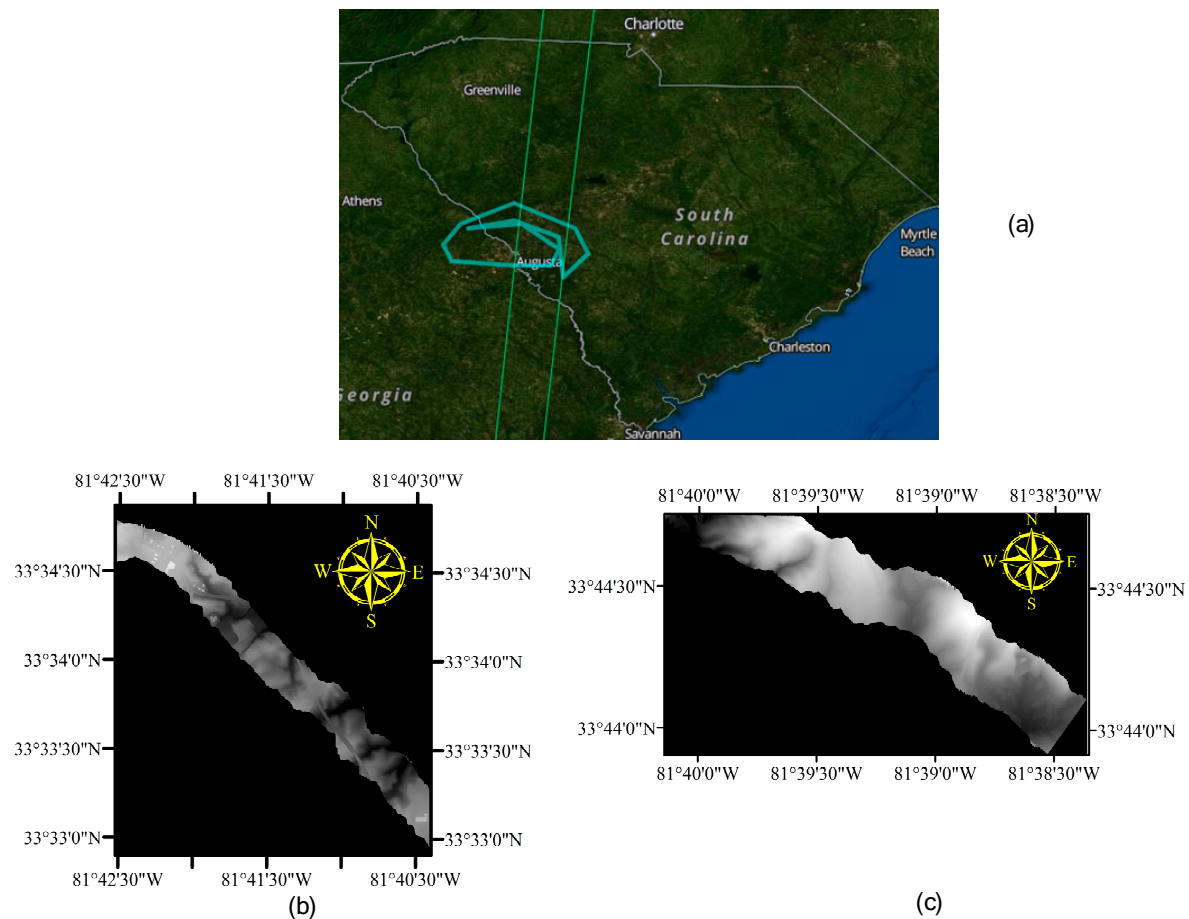


**Figure 3.** (a): Trajectories of Advanced Topographic Laser Altimeter (ATLAS) data (green) and G-LiHT data (blue) depict the location of the study area NASA EARTHDATA. (b): G-LiHT data named AMIGACarb\_Augusta\_FIA\_Sep2011\_116s597\_DTM.tif as reference airborne data. (c): G-LiHT data named AMIGACarb\_Augusta\_FIA\_Sep2011\_140s557\_DTM.tif as reference airborne data.

### 2.3. Methodology

The primary challenge of this contribution centers on reducing the influence of noise photons on the ground elevation data derived from ICESat-2 data, distinguishing canopy signal photons and ground signal photons, and matching the ATL03, ATL08, and G-LiHT data. Although ATLAS data has more noise photons, the NASA official team used the DRAGANN and an algorithm for determining Land Vegetation along-track to provide classification labels (classified\_pc\_flag) for the photon data [43]. In this contribution, the ground signal photon classification label ATL08 is used for ground photons, and the  $DTM_{ATLAS}$  will be established based on ATL03 data and ATL08 label. This contribution presents a quantitative assessment of the ground topography in forested terrain using ATL03 and ATL08 data compared to airborne G-LiHT LiDAR data.

The geolocation between the ATLAS and G-LiHT data is not completely along orbit; therefore, this paper proposes an approach based on the ATL03 profile to match these two datasets (Figure 3).

To clearly illustrate the proposed methodology, an overview of the major steps is exhibited in Figure 4 and described as follows:

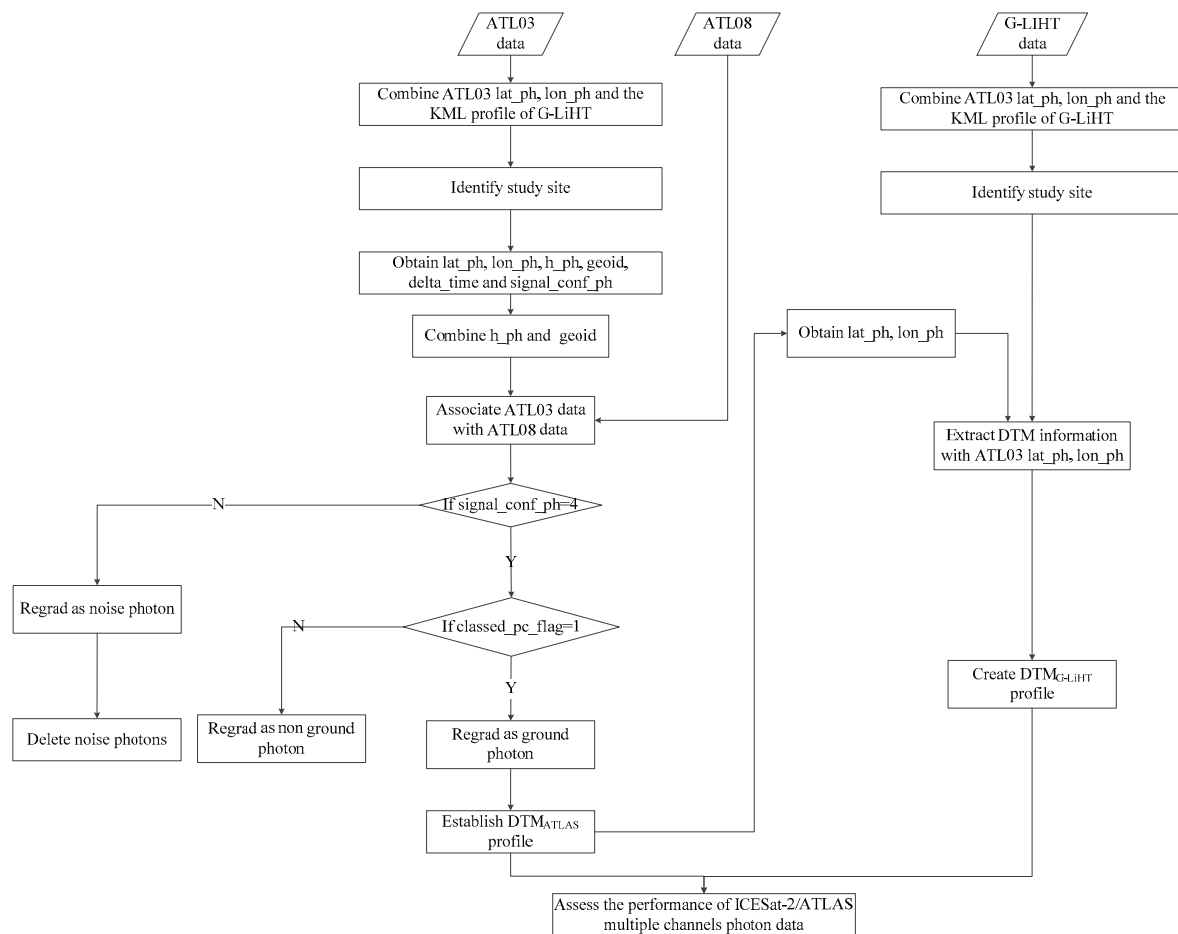


Figure 4. The flowchart of the analysis process.

(1) Identifying study site. In this step, we combine ATL03 lat\_ph, lon\_ph, and G-LiHT KML profile and identify the study site.

(2) Obtain parameters from the ATL03 and ATL08 data by matching different channels under the same orbit conditions using time tags (delta\_time in ATL03 HDF5 profile). To extract the photon's height (h\_ph which is relative to the WGS-84 ellipsoid), latitude (lat\_ph) and longitude (lon\_ph), signal\_conf\_ph, sc\_orient, tx\_pulse\_energy, tx\_pulse\_skew\_est, tx\_pulse\_width\_lower, and tx\_pulse\_width\_upper parameters from the ATL03 HDF5 profile, combine the geoid and h\_ph by interpolating. Extract the photon classification parameters (classed\_pc\_flag), classed\_pc\_indx, and ph\_segment\_id parameters from the ATL08 HDF5 profile.

(3) Establishing the relationship between ATL03 and ATL08 data photon classification parameters by classed\_pc\_indx, ph\_segment\_id and applying each photon classification label from ATL08 to each photon data from ATL03.

(4) Establishing the  $DTM_{ATLAS}$ . The photons with a signal confidence flag from high confidence (signal\_confidence = 4 in ATL03 HDF5 profile) and photon classification parameter (classed\_pc\_flag=1 in ATL08 HDF5 profile) were used to establish the  $DTM_{ATLAS}$ .

(5) Obtaining the  $DTM_{G-LiHT}$ . In this step, we extract the latitude-longitude information from  $DTM_{ATLAS}$  to match the  $DTM_{G-LiHT}$  profile corresponding position generated from G-LiHT and generated  $DTM_{G-LiHT}$  with the corresponding ATLAS footprint latitude-longitude. If the absolute

difference between the elevation of ATLAS ground photons and the corresponding elevation of the  $DTM_{G-LiHT}$  is more than 20 m, this photon was classified as an invalid ground photon.

(6) Assessing the performance of ICESat-2/ATLAS multiple channels photon data. In this final step, we compare the  $DTM_{ATL03}$  profile with the corresponding  $DTM_{G-LiHT}$  profile, compute and analyze the evaluating indicator from different channels. In order to quantify the influence of different laser intensity parameters and laser pointing angle parameters on the estimation accuracy of ground elevation, corresponding four parameters as follow:  $tx\_pulse\_energy$ ,  $tx\_pulse\_skew\_est$ ,  $tx\_pulse\_width\_lower$  and  $tx\_pulse\_width\_upper$  are extracted and analyzed the relationship between the four parameters and elevation errors.

The Figure 5 shows the DTM files of G-LiHT and ATLAS photon data corresponding to the two tracks in the study area. The green dots are ATLAS footprints.

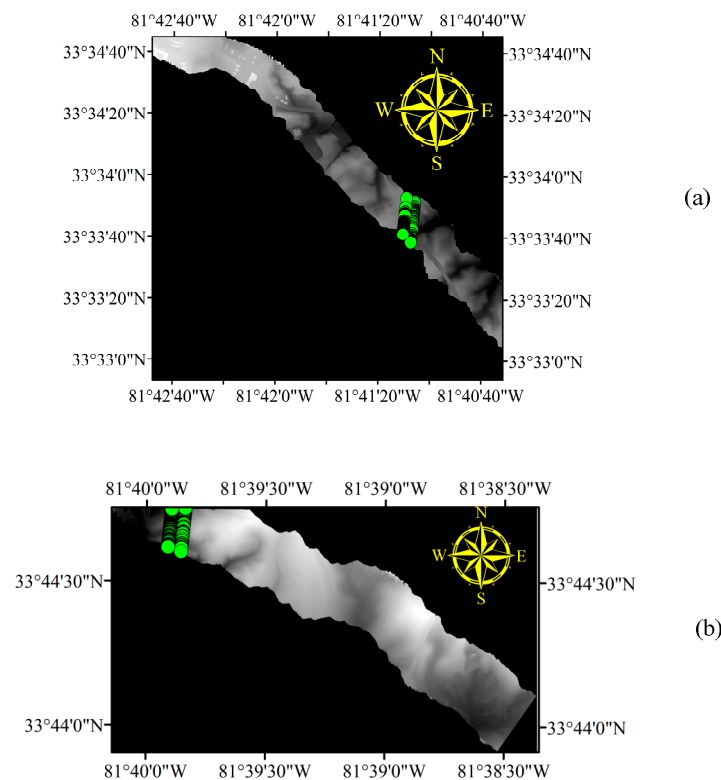


**Figure 5.** Two experimental data (a,b) sets in study area. The green dots on this figure are ATLAS footprints. The gray block is the G-LiHT Digital Terrain Model (DTM).

#### 2.4. Accuracy Evaluation

DTM data derived from airborne G-LiHT LiDAR data were utilized to assess the accuracy of the ATLAS-derived ground elevations. The ground elevation errors in the ATLAS data mentioned in this contribution are calculated by subtracting the G-LiHT elevations from the ATLAS elevations [38]. Seven statistical variables, including root mean squared error (RMSE), mean absolute error (MAE), coefficient of determination ( $R^2$ ), mean error (ME), Pearson correlation coefficient, Spearman correlation coefficient, and Kendall correlation coefficient between the ground elevations and the corresponding G-LiHT's DTM values were calculated to quantitatively evaluate the accuracy of the ATLAS-derived ground elevations. Three statistical variables, Pearson correlation coefficient, Spearman correlation coefficient, and Kendall correlation coefficient between the elevation errors and the corresponding laser intensity parameter and laser pointing angle parameters were calculated to quantitatively evaluate the correlation of laser intensities and laser pointing angles with the elevation error in estimating ground topography in forested terrain.



### 3. Results

#### Result Comparisons

The G-LiHT data in the study was acquired in 2011 and are not temporally coincident with ICESat-2/ATLAS. However, the availability of aerial-based LiDAR data for the study area makes it feasible to validate the ground topography from ATL03. The ATL03 gt3l channel photon data and gt3r channel photon data over the study are plotted with the G-LiHT data shown in Figures 6 and 7, respectively. The scatterplots of the ATL03 (gt3l and gt3r) ground elevations versus the G-LiHT ground elevations are shown in Figures 8 and 9. The statistical indicators, namely the RMSE, MAE,  $R^2$ , ME, Pearson correlation coefficient, Spearman correlation coefficient, and Kendall correlation coefficient are listed in Table 4.

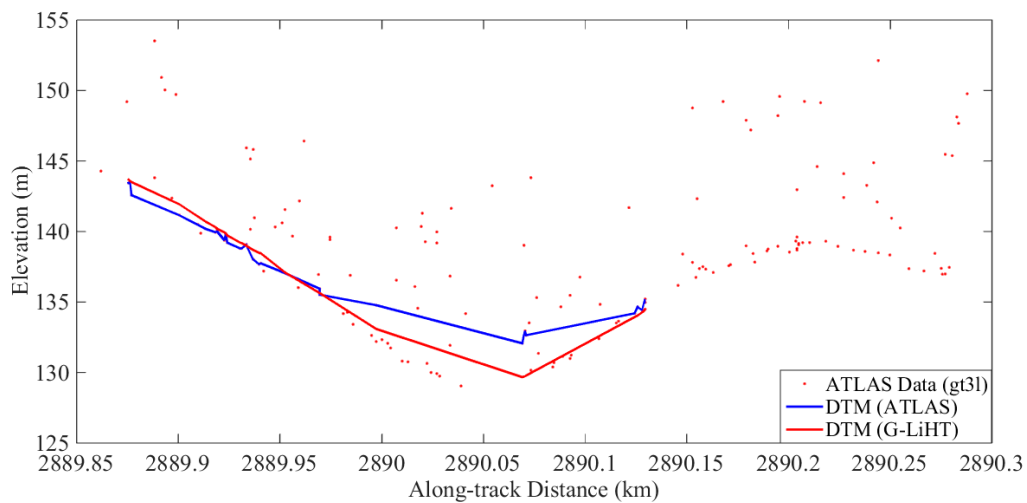


**Figure 6.** A subset of the forested terrain ATL03 (gt3l) ground topography validation results from track ATL03\_20181226053112\_13530106\_001\_01. ATLAS photon data are shown as red dots. The ATLAS DTM (blue line) and the G-LiHT DTM (red line) are also shown.

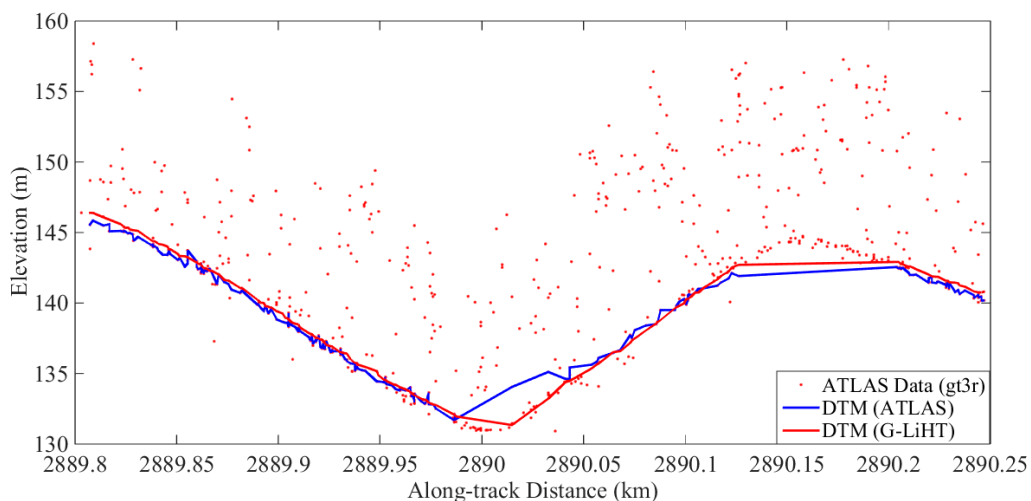


**Figure 7.** A subset of the forested terrain ATL03 (gt3r) ground topography validation results from track ATL03\_20181226053112\_13530106\_001\_01. The ATLAS photon data are shown as red dots. The ATLAS DTM (blue line) and the G-LiHT DTM (red line) are also shown.

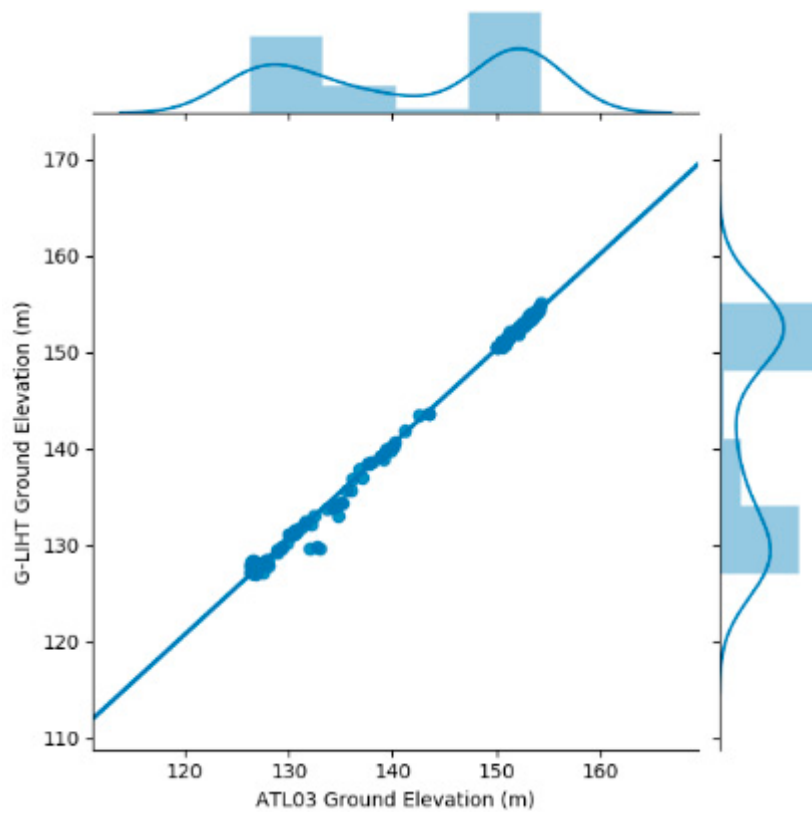


Figure 8. Scatterplot of ATL03 (gt3l) ground topography compared to G-LiHT DTM.

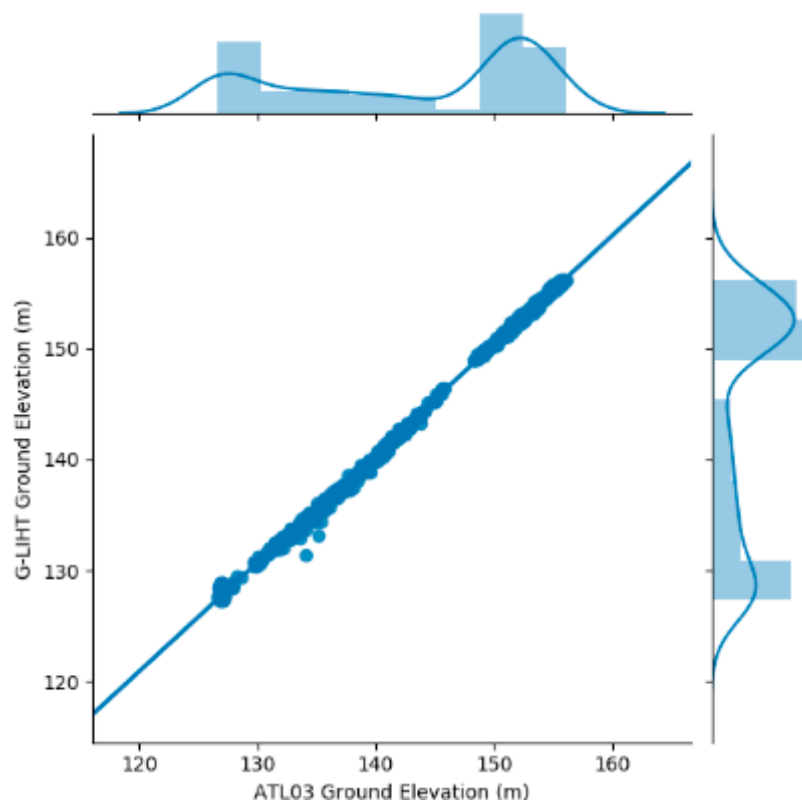


Figure 9. Scatterplot of ATL03 (gt3r) ground topography compared to G-LiHT DTM.

**Table 4.** The statistical indicators of the various laser channels.

Different Laser Channels	RMSE (m)	MAE (m)	R <sup>2</sup>	ME (m)	Pearson	Spearman	Kendall
gt1l	0.69	0.35	1.00	−0.05	1.00	0.99	0.92
gt1r	0.55	0.45	1.00	0.27	1.00	0.99	0.92
gt2l	0.80	0.67	1.00	0.59	1.00	0.96	0.84
gt2r	1.03	0.58	0.99	0.04	1.00	0.99	0.93
gt3l	0.78	0.60	1.00	0.45	1.00	0.99	0.93
gt3r	0.64	0.52	1.00	0.49	1.00	0.99	0.94
Mean of channel	0.75	0.53	1.00	0.30	1.00	0.98	0.91

Note: RMSE—root mean squared error; MAE—mean absolute error; R<sup>2</sup>—coefficient of determination; ME—mean error.

Figures 6 and 7 show the comparisons of elevations from the ATLAS DTM and G-LiHT DTM for multiple channels, and both are referenced to the WGS84 geoid. The ATLAS DTM (blue line) and G-LiHT's DTM (red line) had a similar performance (Figures 6 and 7). The ATLAS gt3l channel (weak beam) photon cloud contains fewer signal photons than the gt3r channel (strong beam). The photons near the blue line and red line denote the ground topography photons. A t-test showed that no significant difference exists between these two regression lines in Figures 8 and 9 at a 95% confidence level. The ATLAS gt3r channel (Figures 7 and 9) signal photons show a clearer depiction of the ground topography than the ATLAS gt3l channel (Figures 6 and 8).

The R<sup>2</sup> of the all experiments are higher than 0.99 (Table 4). The mean ME and RMSE values of all ground photons are 0.3 m and 0.75 m, respectively. For gt1l, gt1r, gt2l, gt2r, gt3l, and gt3r, the ME values are −0.05 m, 0.27 m, 0.59 m, 0.04 m, 0.45 m, and 0.49 m, and the RMSE values are 0.69 m, 0.55 m, 0.80 m, 1.03 m, 0.78 m, and 0.64 m, respectively. In general, the statistical indicators for pointing right (namely strong beam) perform better than those for pointing left (namely weak beam) for all data sets. A possible reason is that the signal photon density from the strong beam channels is significantly higher than that of the weak beam channels.

All laser intensities and laser pointing angles from the ATLO3 product performed well in the study site (Table 4, Figures 8 and 9). The ATLO3 data have good ground elevation estimation accuracy, and the ATLO8 algorithm can effectively filter out noise photon and classify ground photons in the forested terrain ground topography estimation process.

#### 4. Discussion

In order to study the influence of laser intensity and laser pointing angle on ground elevation estimation accuracy, the ATLAS data errors under different laser intensities and laser pointing angles are analyzed respectively, and the correlation between elevation errors and corresponding laser parameters is examined.

##### 4.1. Retrieved Ground Topography in Forested Terrain for Different Laser Intensities

The mean statistical indicators of the different laser intensities are listed in Table 5 and the correlation coefficient statistics between tx\_pulse\_energy parameters and the ATLAS data elevation errors are listed in Table 6.

**Table 5.** Statistical indicators for different laser intensities.

Different Laser Intensities Types	RMSE (m)	MAE(m)	R <sup>2</sup>	ME (m)	Pearson	Spearman	Kendall
Weak beam	0.76	0.54	1.00	0.33	1.00	0.98	0.89
Strong beam	0.74	0.51	1.00	0.27	1.00	0.99	0.93

**Table 6.** Correlation coefficient statistics between tx\_pulse\_energy parameters and ATLAS data. error.

Different Laser Intensities Types	Pearson	Spearman	Kendall
Weak beam	0.58	0.76	0.54
Strong beam	0.59	0.74	0.51
Mean of different laser intensities Types	0.59	0.75	0.53

The estimated ground topography for different intensity beams shows significant agreement with the reference DTM elevations. For the weak beam and strong beam, the mean  $R^2$  values are 1, the ME values are 0.33 m and 0.27 m, and the RMSE values are 0.76 m and 0.74 m, respectively. The correlation coefficient of all types is greater than 0.89.

For the varying laser intensities in this data set, the statistical indicators for the strong beam performed better than that of weak beam with the lower RMSE ( $RMSE_{\text{strong beam}} = 0.74$  m and  $RMSE_{\text{weak beam}} = 0.76$  m), lower MAE ( $MAE_{\text{strong beam}} = 0.51$  m and  $MAE_{\text{weak beam}} = 0.54$  m), lower ME ( $ME_{\text{strong beam}} = 0.33$  m and  $ME_{\text{weak beam}} = 0.27$  m), and higher correlation coefficient. A possible reason is that the weak beam channel has fewer signal photons compared to the strong channel, making measuring ground topography in forested terrain using the weak beam more difficult. Using a strong beam, ATLAS could produce more signal photons than under the weak beam. The laser intensity ratio of strong beam to weak beam is 4:1. Depending upon the surface reflectance and atmospheric conditions, up to 16 photons per outgoing shot could be detected for the strong beam, while the weak beam could detect only 4 photons. However, the strong and weak beams can both provide useable data for measuring ground topography in forested terrain.

To further explore the influence of laser intensities on elevation errors, we calculated three correlation coefficients between tx\_pulse\_energy parameters and elevation errors (Table 6). For all the data, the correlation coefficients for the elevation errors and tx\_pulse\_energy parameters are greater than 0.5. In addition, the Spearman correlation coefficient values for the various laser intensities are greater than 0.74, indicating there is a significant correlation between the tx\_pulse\_energy parameters and elevation error. However, this contribution only explores the correlation between tx\_pulse\_energy and elevation error for a laser intensity ranging from 0.02 mJ to 0.09 mJ. Future studies with the tx\_pulse\_energy parameters will need to perform a more detailed analysis on the effect of tx\_pulse\_energy on elevation error.

Compared to the forested terrain ground topography estimation method in proposed by Neuenschwander et al. [37], higher  $R^2$  values and lower RMSE values were observed in the strong beam mode and weak beam mode. However, this study proposes a photon level which is different to the Neuenschwander et al. method [37], which notes that the result of a photon subset using a strong beam and a weak beam can reasonably explain the ground topography in the forest study area.

#### 4.2. Retrieved Ground Topography in Forested Terrain Elevation with Different Laser Pointing Angles

The mean statistical indicators for the different laser pointing angles are listed in Table 7 and the correlation coefficient statistics between tx\_pulse\_skew\_est, tx\_pulse\_width\_lower, tx\_pulse\_width\_upper parameters and the elevation errors of ATLAS data are listed in Table 8.

**Table 7.** The statistical indicators for different laser pointing angles.

Different Laser Channels	RMSE (m)	MAE(m)	$R^2$	ME (m)	Pearson	Spearman	Kendall
gt1	0.62	0.40	1.00	0.11	1.00	0.99	0.92
gt2	0.92	0.62	1.00	0.31	1.00	0.97	0.88
gt3	0.71	0.56	1.00	0.47	1.00	0.99	0.93

**Table 8.** The correlation coefficient statistics between tx\_pulse\_skew\_est, tx\_pulse\_width\_lower, tx\_pulse\_width\_upper parameters and the elevation errors of ATLAS data.

Statistical Indicators	Different Laser Pointing Angles	Pearson	Spearman	Kendall
tx_pulse_skew_est	gt1	0.12	0.05	0.04
	gt2	0.11	0.21	0.12
	gt3	0.15	0.15	0.11
	Mean of different pointings	0.13	0.14	0.09
tx_pulse_width_lower	gt1	0.20	0.10	0.07
	gt2	0.10	0.07	0.05
	gt3	0.20	0.21	0.14
	Mean of different pointings	0.17	0.13	0.09
tx_pulse_width_upper	gt1	0.24	0.31	0.23
	gt2	0.09	0.12	0.09
	gt3	0.11	0.13	0.09
	Mean of different pointings	0.15	0.19	0.14

The estimated ground topography in forested terrain using different laser pointing angles shows strong agreement with the reference DTM<sub>G-LiHT</sub> elevations, as demonstrated by the  $R^2$  values equaling 1.00 and the RMSE values less than 0.92 m.

Results indicated that the gt1 channel pointing ( $R^2_{gt1\ channel} = 1.00$ ,  $RMSE_{gt1\ channel} = 0.62$  m,  $MAE_{gt1\ channel} = 0.4$  m) performed better than gt2 channel pointing ( $R^2_{gt2\ channel} = 1.00$ ,  $RMSE_{gt2\ channel} = 0.92$  m,  $MAE_{gt2\ channel} = 0.62$  m) and gt3 channel pointing ( $R^2_{gt3\ channel} = 1.00$ ,  $RMSE_{gt3\ channel} = 0.71$  m,  $MAE_{gt3\ channel} = 0.56$  m), which was due to several hardware reasons. On one hand, the gt1 channel could achieve more effective forested terrain signal photons than other channels in the study area. More signal photons can give a clearer depiction of ground topography in forested terrain. On the other hand, the photon rates of the gt1 and gt3 channels are higher than the gt2 channel, which is consistent with the description of the different laser pointing angles [46].

To further explore the influence of laser pointing angles on elevation error, we calculated three correlation coefficients between tx\_pulse\_skew\_est, tx\_pulse\_width\_lower, tx\_pulse\_width\_upper parameters and elevation error. In the ATL03 Algorithm Theoretical Basis Document (ATBD), these parameters may be related to the laser pointing angles. The quantitative results of the correlation coefficients are summarized in Table 8. For all the data, the mean correlation coefficients for the elevation errors are less than 0.20. There is no significant correlation between the tx\_pulse\_skew\_est, tx\_pulse\_width\_lower, tx\_pulse\_width\_upper parameters and the elevation error. However, this contribution only explores the correlation between tx\_pulse\_skew\_est, tx\_pulse\_width\_lower, tx\_pulse\_width\_upper and the elevation error. Future studies needed to analyze other laser pointing angles parameters' relative elevation errors.

The results of this contribution performed better than that proposed by Neuenschwander et al. [37] ( $R^2 = 0.99$ ,  $RMSE = 0.85$ ), which notes that the result of a photon subset using different laser pointing angles can reasonably explain the ground topography in the study area.

#### 4.3. Retrieved Ground Topography in Forested Terrain Elevation with ATLAS

Most optical remote sensing systems could provide images of the horizontal distribution of ground topography, and the product generally follows the uppermost surface elevation (i.e., representing a digital surface model, DSM). However, the optical remote sensing images do not provide detailed information on the vertical distribution of ground topography in forested terrain, without regard to whether the surface is comprised of forest or not [5,6,47]. In contrast, the LiDAR photon counting signature from ICESat-2/ATLAS could provide a direct depiction for ground topography in forested terrain. In this contribution, the close correspondence between the ATLAS and G-LiHT ( $R^2 = 1.00$ ,  $RMSE = 0.75$  m) confirms that the received photon data are an accurate representation of the ground



topography forested terrain elevation within the ATLAS footprints. As a comparison, in areas of low relief (slope  $\leq 5^\circ$ ) and middle dense tree cover (tree cover = 20%–40%), the mean and standard deviation of elevation differences between the ICESat/GLAS centroid and SRTM are  $-2.48 \pm 4.04$  m [48]. Thus, the estimation of ground topography for forest-covered areas is able to be accomplished with ICESat-2/ATLAS.

The results from this contribution indicate that the ground topography in forested terrain elevation can be estimated using photon data from ICESat-2/ATLAS multi-channel. We were able to retrieve terrain elevation successfully in forest-covered areas. Prior work showing the correlation between spaceborne LiDAR-measured canopy height and ground topography in forested terrain [21–23], which provide confidence that ICESat-2/ATLAS photon data in combination with GEDI data can substantially contribute to a global inventory of forest biomass. The work also provides insights for future work to improve the accuracy of the canopy height estimations.

## 5. Conclusions

In this contribution, ICESat-2 data is used to measure ground topography in forested terrain using different channels. The retrieved ground topography was validated by experiments with G-LiHT airborne data at different laser pointing angles and laser intensity types on the same route. Based on the results, the following conclusions can be drawn:

(1) Both qualitative and quantitative results indicate that at all laser intensities and laser pointing types resulted in a mean  $R^2 = 1.00$  and mean RMSE = 0.75 m, highlighting the ability of the ATL03 and ATL08 data to retrieve ground elevations.

(2) A significant correlation exists between the tx\_pulse\_energy parameters and elevation error. There is no significant correlation between tx\_pulse\_skew\_est, tx\_pulse\_width\_lower, tx\_pulse\_width\_upper parameters and elevation error.

These conclusions give valuable insight into the ground topography in forested terrain using different ATLAS channels. Nevertheless, there are still many issues to be addressed in the future. Since ATLAS data is still in the research stage, we only considered the effects of laser pointing angles and laser intensity on retrieving ground topography. Other factors (e.g., canopy height, canopy cover, etc.) influencing the results were not considered. Therefore, the effects of other factors on retrieving ground topography over forested terrain using ATLAS data should be thoroughly examined in the future.

**Author Contributions:** J.H., Y.X. and L.Q. conceived and designed the experiments; J.H. performed the experiments; J.H. and Y.X. analyzed the data; L.Q. contributed materials; J.H., Y.X. and A.G. wrote the paper; Y.X. secured funding for the project; A.G. polished the language of the manuscript. All authors have read and agreed to the published version of the manuscript.

**Funding:** This work is supported by the National Key R&D Program of China (Grant Number: 2017YFD0600904), the Fundamental Research Funds for the Central Universities (Grant Number:2572019AB18), and the Key Laboratory of Satellite Mapping Technology and Application, National Administration of Surveying, Mapping and Geoinformation (KLSMTA-201706).

**Acknowledgments:** We thank the editor and anonymous reviewers for reviewing our paper.

**Conflicts of Interest:** The authors declare no conflict of interest.

## References

1. Thom, D.; Keeton, W.S. Stand structure drives disparities in carbon storage in northern hardwood-conifer forests. *For. Ecol. Manag.* **2019**, *442*, 10–20. [[CrossRef](#)]
2. Ferreira, A.C.; Bezerra, L.E.A.; Cascon, H.M. Aboveground carbon stock in a restored neotropical mangrove: Influence of management and brachyuran crab assemblage. *Wetl. Ecol. Manag.* **2019**, *27*, 223–242. [[CrossRef](#)]
3. Quegan, S.; le Toan, T.; Chave, J.; Dall, J.; Exbrayat, J.F.; Minh, D.H.T.; Lomas, M.; d’Alessandro, M.M.; Paillou, P.; Papathanassiou, K.; et al. The European Space Agency BIOMASS mission: Measuring forest above-ground biomass from space. *Remote Sens. Environ.* **2019**, *227*, 44–60. [[CrossRef](#)]

4. Ni, W.; Zhang, Z.; Sun, G.; Liu, Q. Modeling the Stereoscopic Features of Mountainous Forest Landscapes for the Extraction of Forest Heights from Stereo Imagery. *Remote Sens.* **2019**, *11*, 1222. [[CrossRef](#)]
5. Hu, T.; Su, Y.; Xue, B.; Liu, J.; Zhao, X.; Fang, J.; Guo, Q. Mapping Global Forest Aboveground Biomass with Spaceborne LiDAR, Optical Imagery, and Forest Inventory Data. *Remote Sens.* **2016**, *8*, 565. [[CrossRef](#)]
6. Wang, S.; Ren, Z.; Wu, C.; Lei, Q.; Gong, W.; Ou, Q.; Zhang, H.; Ren, G.; Li, C. DEM generation from Worldview-2 stereo imagery and vertical accuracy assessment for its application in active tectonics. *Geomorphology* **2019**, *336*, 107–118. [[CrossRef](#)]
7. Yu, Y.; Yang, X.G.; Fan, W.Y. Estimates of forest structure parameters from GLAS data and multi-angle imaging spectrometer data. *Int. J. Appl. Earth Obs. Geoinf.* **2015**, *38*, 65–71. [[CrossRef](#)]
8. Zhao, F.; Yang, X.Y.; Strahler, A.H.; Schaaf, C.L.; Yao, T.; Wang, Z.S.; Román, M.O.; Woodcock, C.E.; Ni-Meister, W.; Jupp, D.L.B.; et al. A comparison of foliage profiles in the Sierra National Forest obtained with a full-waveform under-canopy EVI lidar system with the foliage profiles obtained with an airborne full-waveform LVIS lidar system. *Remote Sens. Environ.* **2013**, *136*, 330–341. [[CrossRef](#)]
9. Bouvier, M.; Durrieu, S.; Fournier, R.A.; Renaud, J.P. Generalizing predictive models of forest inventory attributes using an area-based approach with airborne LiDAR data. *Remote Sens. Environ.* **2015**, *156*, 322–334. [[CrossRef](#)]
10. Dandois, J.P.; Ellis, E.C. High spatial resolution three-dimensional mapping of vegetation spectral dynamics using computer vision. *Remote Sens. Environ.* **2013**, *136*, 259–276. [[CrossRef](#)]
11. Disney, M.; Burt, A.; Calders, K.; Schaaf, C.; Stovall, A. Innovations in Ground and Airborne Technologies as Reference and for Training and Validation: Terrestrial Laser Scanning (TLS). *Surv. Geophys.* **2019**, *40*, 937–958. [[CrossRef](#)]
12. Disney, M. Terrestrial LiDAR: A three-dimensional revolution in how we look at trees. *N. Phytol.* **2019**, *222*, 1736–1741. [[CrossRef](#)] [[PubMed](#)]
13. Wijesingha, J.; Moeckel, T.; Hensgen, F.; Wachendorf, M. Evaluation of 3D point cloud-based models for the prediction of grassland biomass. *Int. J. Appl. Earth Obs. Geoinf.* **2019**, *78*, 352–359. [[CrossRef](#)]
14. Schneider, F.D.; Kükenbrink, D.; Schaepman, M.E.; Schimel, D.S.; Morsdorf, F. Quantifying 3D structure and occlusion in dense tropical and temperate forests using close-range LiDAR. *Agric. For. Meteorol.* **2019**, *268*, 249–257. [[CrossRef](#)]
15. Bakx, T.R.; Koma, Z.; Seijmonsbergen, A.C.; Kissling, W.D. Use and categorization of Light Detection and Ranging vegetation metrics in avian diversity and species distribution research. *Divers. Distrib.* **2019**, *25*, 1045–1059. [[CrossRef](#)]
16. Zwally, H.J.; Schutz, B.; Abdalati, W.; Abshire, J.; Bentley, C.; Brenner, A.; Bufton, J.; Dezio, J.; Hancock, D.; Harding, D.; et al. ICESat's laser measurements of polar ice, atmosphere, ocean, and land. *J. Geodyn.* **2002**, *34*, 405–445. [[CrossRef](#)]
17. Kellner, J.R.; Armston, J.; Birrer, M.; Cushman, K.C.; Duncanson, L.; Eck, C.; Fallegger, C.; Imbach, B.; Král, K.; Krůček, M.; et al. New Opportunities for Forest Remote Sensing Through Ultra-High-Density Drone Lidar. *Surv. Geophys.* **2019**, *40*, 959–977. [[CrossRef](#)]
18. Popescu, S.C.; Zhou, T.; Nelson, R.; Neuenschwander, A.; Sheridan, R.; Narine, L.; Walsh, K.M. Photon counting LiDAR: An adaptive ground and canopy height retrieval algorithm for ICESat-2 data. *Remote Sens. Environ.* **2018**, *208*, 154–170. [[CrossRef](#)]
19. Wang, Y.; Ni, W.; Sun, G.; Chi, H.; Zhang, Z.; Guo, Z. Slope-adaptive waveform metrics of large footprint lidar for estimation of forest aboveground biomass. *Remote Sens. Environ.* **2019**, *224*, 386–400. [[CrossRef](#)]
20. Harding, D.J.; Carabajal, C.C. ICESat waveform measurements of within footprint topographic relief and vegetation vertical structure. *Geophys. Res. Lett.* **2005**, *32*, L21S10. [[CrossRef](#)]
21. Lefsky, M.A.; Harding, D.J.; Keller, M.; Cohen, W.B.; Carabajal, C.C.; Espirito-Santo, F.D.B.; Hunter, M.O.; de Oliveira, R., Jr. Estimates of forest canopy height and above ground biomass using ICESat. *Geophys. Res. Lett.* **2005**, *32*, L22S02. [[CrossRef](#)]
22. Chen, Q. Assessment of terrain elevation derived from satellite laser altimetry over mountainous forest areas using airborne lidar data. *ISPRS J. Photogramm. Remote Sens.* **2010**, *65*, 111–122. [[CrossRef](#)]
23. Fang, Z.; Cao, C.X. Estimation of Forest Canopy Height Over Mountainous Areas Using Satellite Lidar. *IEEE J. Sel. Top. Appl. Earth Obs. Remote Sens.* **2014**, *7*, 3157–3166. [[CrossRef](#)]

24. Lee, S.; Ni-Meister, W.; Yang, W.; Chen, Q. Physically based vertical vegetation structure retrieval from ICESat data: Validation using LVIS in White Mountain National Forest, New Hampshire, USA. *Remote Sens. Environ.* **2011**, *115*, 2776–2785. [[CrossRef](#)]
25. Claudia, H.; Christiane, S. Influence of Surface Topography on ICESat/GLAS Forest Height Estimation and Waveform Shape. *Remote Sens.* **2012**, *4*, 2210–2235. [[CrossRef](#)]
26. Saarela, S.; Holm, S.; Healey, S.P.; Andersen, H.-E.; Petersson, H.; Prentius, W.; Patterson, P.L.; Næsset, E.; Gregoire, T.G.; Ståhl, G. Generalized Hierarchical Model-Based Estimation for Aboveground Biomass Assessment Using GEDI and Landsat Data. *Remote Sens.* **2018**, *10*, 1832. [[CrossRef](#)]
27. Markus, T.; Neumann, T.; Martino, A.; Abdalati, W.; Brunt, K.; Csatho, B.; Farrell, S.; Fricker, H.; Gardner, A.; Harding, D.; et al. The Ice, Cloud, and land Elevation Satellite-2 (ICESat-2): Science requirements, concept, and implementation. *Remote Sens. Environ.* **2017**, *190*, 260–273. [[CrossRef](#)]
28. Brunt, K.M.; Neumann, T.A.; Walsh, K.M.; Markus, T. Determination of Local Slope on the Greenland Ice Sheet Using a Multibeam Photon-Counting Lidar in Preparation for the ICESat-2 Mission. *IEEE Geosci. Remote Sens. Lett.* **2014**, *11*, 935–939. [[CrossRef](#)]
29. Magruder, L.A.; Brunt, K.M. Performance Analysis of Airborne Photon Counting Lidar Data in Preparation for the ICESat-2 Mission. *IEEE Trans. Geosci. Remote Sens.* **2018**, *56*, 2911–2918. [[CrossRef](#)]
30. Ma, Y.; Li, S.; Zhang, W.; Zhang, Z.; Liu, R.; Wang, X.H. Theoretical ranging performance model and range walk error correction for photon counting lidars with multiple detectors. *Opt. Express* **2018**, *26*, 15924–15934. [[CrossRef](#)]
31. Li, S.; Zhang, Z.; Ma, Y.; Zeng, H.; Zhao, P.; Zhang, W. Ranging performance models based on negative-binomial (NB) distribution for photon-counting lidars. *Opt. Express* **2019**, *27*, A861–A877. [[CrossRef](#)] [[PubMed](#)]
32. Ma, Y.; Liu, R.; Li, S.; Zhang, W.; Yang, F.; Su, D. Detecting the ocean surface from the raw data of the MABEL photon-counting lidar. *Opt. Express* **2018**, *26*, 24752–24762. [[CrossRef](#)] [[PubMed](#)]
33. Neuenschwander, A.L.; Magruder, L.A. The Potential Impact of Vertical Sampling Uncertainty on ICESat-2/ATLAS Terrain and Canopy Height Retrievals for Multiple Ecosystems. *Remote Sens.* **2016**, *8*, 1039. [[CrossRef](#)]
34. Abdalati, W.; Zwally, H.J.; Bindschadler, R.; Csatho, B.; Farrell, S.L.; Fricker, H.A.; Harding, D.; Kwok, R.; Lefsky, M.; Markus, T.; et al. ICESat-2 Laser Altimetry Mission. *Proc. IEEE* **2010**, *98*, 735–751. [[CrossRef](#)]
35. Nie, S.; Wang, C.; Xi, X.; Luo, S.; Li, G.; Tian, J.; Wang, H. Estimating the vegetation canopy height using micro-pulse photon-counting LiDAR data. *Opt. Express* **2018**, *26*, A520–A540. [[CrossRef](#)]
36. Narine, L.L.; Popescu, S.C.; Malambo, L. Synergy of ICESat-2 and Landsat for Mapping Forest Aboveground Biomass with Deep Learning. *Remote Sens.* **2019**, *11*, 1503. [[CrossRef](#)]
37. Neuenschwander, A.L.; Magruder, L.A. Canopy and Terrain Height Retrievals with ICESat-2: A First Look. *Remote Sens.* **2019**, *11*, 1721. [[CrossRef](#)]
38. Wang, C.; Zhu, X.; Nie, S.; Xi, X.; Li, D.; Zheng, W.; Chen, S. Ground elevation accuracy verification of ICESat-2 data: A case study in Alaska, USA. *Opt. Express.* **2019**, *27*, 38168–38179. [[CrossRef](#)]
39. Neumann, T.; Brenner, A.; Hancock, D.; Robbins, J.; Saba, J.; Harbeck, K.; Gibbons, A. *ICE, CLOUD, and Land Elevation Satellite-2(ICESat-2) Project Algorithm Theoretical Basis Document (ATBD) for Global Geolocated Photons ATLO3*; National Aeronautics and Space Administration: Washington, DC, USA; Goddard Space Flight Centre: Greenbelt, MD, USA, 2018.
40. Harrington, T.B.; Edwards, M.B. Understory vegetation, resource availability, and litterfall responses to pine thinning and woody vegetation control in longleaf pine plantations. *Can. J. For. Res.* **1999**, *29*, 1055–1064. [[CrossRef](#)]
41. Huang, J.P.; Xing, Y.Q.; You, H.T.; Qin, L.; Tian, J.; Ma, J.M. Particle Swarm Optimization-Based Noise Filtering Algorithm for Photon Cloud Data in Forest Area. *Remote Sens.* **2019**, *11*, 980. [[CrossRef](#)]
42. Neuenschwander, A.; Popescu, S.; Nelson, R.; Harding, D.; Pitts, K.; Robbins, J.; Pederson, D.; Sheridan, R. *ICE, CLOUD, and Land Elevation Satellite (ICESat-2) Algorithm Theoretical Basis Document (ATBD) for Land-Vegetation Along-Track Products*; National Aeronautics and Space Administration: Washington, DC, USA; Goddard Space Flight Centre: Greenbelt, MD, USA, 2019.
43. Neumann, T.; Brenner, A.; Hancock, D.; Luthcke, S.; Lee, J.; Robbins, J.; Harbeck, K.; Saba, J.; Brunt, K. *ATLAS/ICESat-2 L2A Global Geolocated Photon Data, Version 2*; NSIDC National Snow and Ice Data Center: Boulder, CO, USA, 2019.

44. Cook, B.D.; Corp, L.A.; Nelson, R.F.; Middleton, E.M.; Morton, D.C.; McCorkel, J.T.; Masek, J.G.; Ranson, K.J.; Ly, V.; Montesano, P.M. NASA Goddard's LiDAR, Hyperspectral and Thermal (G-LiHT) Airborne Imager. *Remote Sens.* **2013**, *5*, 4045–4066. [[CrossRef](#)]
45. Chen, B.; Pang, Y.; Li, Z.; North, P.; Rosette, J.; Sun, G.; Suárez, J.; Bye, I.; Lu, H. Potential of Forest Parameter Estimation Using Metrics from Photon Counting LiDAR Data in Howland Research Forest. *Remote Sens.* **2019**, *11*, 856. [[CrossRef](#)]
46. Kwok, R.; Markus, T.; Kurtz, N.T.; Petty, A.A.; Farrell, T.A.N.S.L.; Cunningham, G.F.; Hancock, D.W.; Ivanoff, A.; Wimert, J.T. Surface Height and Sea Ice Freeboard of the Arctic Ocean From ICESat-2: Characteristics and Early Results. *J. Geophys. Res. Oceans* **2019**, *124*. [[CrossRef](#)]
47. Meddens, A.J.; Vierling, L.A.; Eitel, J.U.; Jennewein, J.S.; White, J.C.; Wulder, M.A. Developing 5 m resolution canopy height and digital terrain models from WorldView and ArcticDEM data. *Remote Sens. Environ.* **2018**, *218*, 174–188. [[CrossRef](#)]
48. Carabajal, C.C.; Harding, D.J. ICESat validation of SRTM C-band digital elevation models. *Geophys. Res. Lett.* **2005**, *32*, L22S01. [[CrossRef](#)]



© 2020 by the authors. Licensee MDPI, Basel, Switzerland. This article is an open access article distributed under the terms and conditions of the Creative Commons Attribution (CC BY) license (<http://creativecommons.org/licenses/by/4.0/>).